

# A simple microscopic description of quantum Hall transition without Landau levels

V. V. Mkhitarian<sup>1</sup>, V. Kagalovsky<sup>2</sup>, and M. E. Raikh<sup>1</sup>

<sup>1</sup>*Department of Physics, University of Utah, Salt Lake City, UT 84112, USA*

<sup>2</sup>*Sami Shamoon College of Engineering, Beer Sheva 84100, Israel*

By restricting the motion of high-mobility 2D electron gas to a network of channels with smooth confinement, we were able to trace, both classically and quantum-mechanically, the interplay of backscattering, and of the bending action of a weak magnetic field. Backscattering limits the mobility, while bending initiates quantization of the Hall conductivity. We demonstrate that, in restricted geometry, electron motion reduces to *two* Chalker-Coddington networks, with *opposite* directions of propagation along the links, which are weakly coupled by disorder. Interplay of backscattering and bending results in the quantum Hall transition in a *non-quantizing* magnetic field, which decreases with increasing mobility. This is in accord with scenario of floating up delocalized states.

PACS numbers: 72.15.Rn; 73.20.Fz; 73.43.-f

*Introduction.* Quantization of the Hall conductivity of a disordered 2D electron gas,  $\sigma_{xy} = n$ , (in the units of  $e^2/h$ ) together with vanishing diagonal conductivity,  $\sigma_{xx}$ , reflect the fact that in a perpendicular magnetic field delocalized states always constitute a discrete set, as was first argued in Ref. 1.

In a strong magnetic field,  $\omega_c\tau \gg 1$ , where  $\omega_c$  is a cyclotron frequency and  $\tau$  is the scattering time, energy positions,  $E_n$ , of the delocalized states coincide with the centers of well-resolved Landau bands. For this reason the vast majority of theoretical approaches to delocalization in a magnetic field focus on the situation when the Fermi level crosses certain  $E_n$  upon changing either magnetic field or electron density. Most appealing qualitative picture [2] assumes a smooth disorder when the eigenstates are well-defined Larmor circles drifting along equipotential lines. Then delocalization corresponds to the *classical* percolation threshold; localized states above  $E_n$  are closed drift trajectories executed, *e.g.*, clockwise, while the states below  $E_n$  are closed drift trajectories executed counter-clockwise, see Fig. 1.

An alternative approach [3] to delocalization is based on renormalization-group equations, describing the evolution of  $\sigma_{xx}$ ,  $\sigma_{xy}$  upon increasing the sample size,  $L$ ,

$$\frac{\partial \sigma_{xx}}{\partial \ln L} = -\frac{1}{2\pi^2 \sigma_{xx}} - \sigma_{xx} D e^{-2\pi \sigma_{xx}} \cos(2\pi \sigma_{xy}), \quad (1)$$

$$\frac{\partial \sigma_{xy}}{\partial \ln L} = -\sigma_{xx} D e^{-2\pi \sigma_{xx}} \sin(2\pi \sigma_{xy}), \quad (2)$$

where  $D$  is a dimensionless constant. First term of Eq. (1) originates from *interference* of electron multiple-scattering paths: two paths corresponding to the *same* scatterers but different sequences of scattering events interfere even in the presence of Aharonov-Bohm phases. Second term reflects the *orbital* action of magnetic field: by curving electron trajectories it tends to destroy the interference. When the “phase” and “orbital” terms compensate each other, delocalization transition takes place.

Field-theoretical approach [3] yields a highly nontrivial prediction first pointed out by Khmelnitskii [4]. Namely,

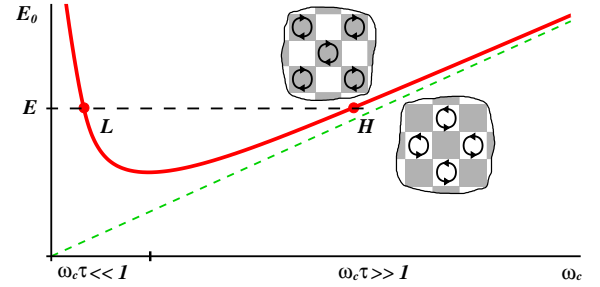


FIG. 1: (Color online) Energy position of the lowest delocalized state,  $E_0$ , vs. magnetic field,  $\omega_c$ , as predicted in Ref. 4. For a given  $E$ , delocalization transition occurs at points  $L$  and  $H$ . Change of character of electron motion near  $H$  is illustrated schematically. Corresponding change near  $L$  is illustrated in Fig. 4 ( $a \leftrightarrow e$ ).

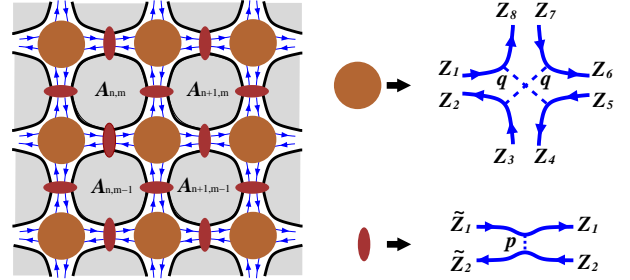


FIG. 2: (Color online) Left: Restricted electron motion over point contacts and bend-junctions is illustrated;  $A_{n,m}$  are the centers of forbidden regions. Right: Scattering matrices of the junction and of the point contact.

solving Eqs. (1), (2) together with classical initial condition  $\sigma_{xy}(\omega_c) = \sigma_0 \omega_c \tau (1 + \omega_c^2 \tau^2)^{-1}$ , where  $\sigma_0 \propto E_n$  is the dimensionless conductance at  $\omega_c = 0$ , yields  $E_n = \hbar \omega_c (n + \frac{1}{2}) [1 + (\omega_c \tau)^{-2}]$ . As shown in Fig. 1 for  $n = 0$ , the high-field part,  $\omega_c \tau \gg 1$ , of  $E_0$  follows the center of the lowest Landau level, while the low-field part “floats up” as  $\omega_c \tau \rightarrow 0$ .

Qualitative classical picture [2] applies to the high-field part and illustrates the restructuring, see Fig. 1, of the

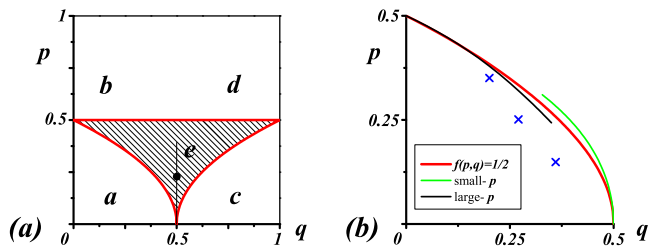


FIG. 3: (Color online) (a) Classical metallic phase, dashed region (e) in the  $(p, q)$ -plane separates different insulating phases of the model Fig. 2; (b) Line of classical delocalization transitions in the  $(p, q)$ -plane. Small- $p$  and small- $q$  asymptotes calculated from Eqs. (5), (7), are shown with green and black lines, respectively; red curve interpolates the threshold position between the two regimes. Crosses show the positions of quantum delocalization transition inferred from simulations for three values of “energies”,  $p$ .

motion of guiding center, which accompanies the crossing of  $E_0$  by the Fermi level,  $E_F$ , upon increasing magnetic field ( $1 \rightarrow 0$  transition).

While there is certain experimental evidence [5, 6, 7, 8, 9, 10, 11] that floating up of  $E_0(\omega_c)$  indeed takes place, tight-binding numerical studies [12, 13, 14] are less conclusive. There is a fundamental reason [15] for this lack of conclusiveness. Indeed, significant floating up occurs for large  $\sigma_0 > (\omega_c \tau)^{-1} \gg 1$ . For such  $\sigma_0$ , upon moving along the dashed horizontal line in Fig. 1 the localization length undergoes a steep growth from orthogonal value  $\xi_o \sim \exp(\pi \sigma_0)$  to the unitary value  $\xi_u \sim \exp(\pi^2 \sigma_0^2)$  already in very small fields  $\omega_c \tau \simeq \sigma_0^{-1} e^{-2\pi \sigma_0}$ , way before the expected transition at point  $L$ . In view of such high  $\xi_u$  the best what numerics, restricted to finite size samples, can reveal is the transition between quantum Hall insulator and a metal taking place around the point  $L$ . There remains a major challenge to come up with a microscopic picture of this transition, as transparent as the picture [2] reproduced near the point  $H$  in Fig. 1. Unlike Ref. 2, such a picture should not invoke the language of equipotentials and fully chiral motion; this language is inadequate at low fields. In the present paper we construct the corresponding picture. The key step of this construction is separation of the spatial regions with disorder-induced scattering and field-induced bending.

*Restricted electron motion.* (i) In contrast to unidirectional motion in strong fields, we allow counter-propagating paths in the regions where *orbital* action of magnetic field is negligible. We achieve this by restricting electrons to narrow point contacts, see Fig. 2. At the same time, we assume that the *phase* action of magnetic field is well-developed in each point contact, i.e., the area of the contact is threaded by many flux quanta. Presence of disorder is incorporated by allowing mutual backscattering of two counterpropagating waves. We quantify the

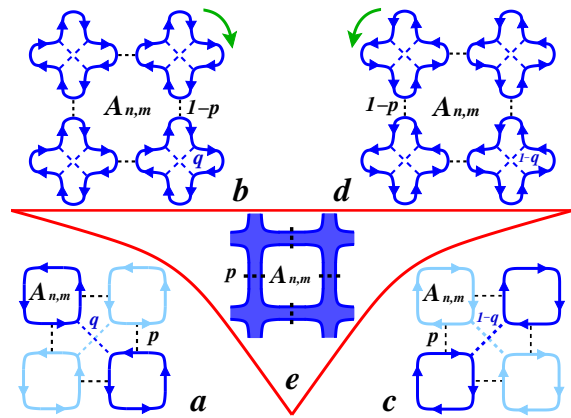


FIG. 4: (Color online) Illustration of the structure of five different phases in Fig. 3. Electron moves predominantly along solid directed lines. In phases  $a$  and  $c$  the motion is either within dark or within light subnetwork. In phase  $e$  coupling of subnetworks by  $p$ -bonds opens a metallic phase.

strength of backscattering with probability,  $p$ , so that the scattering matrix of the contact has the form

$$\begin{pmatrix} Z_1 \\ \tilde{Z}_2 \end{pmatrix} = \begin{pmatrix} \sqrt{1-p} & \sqrt{p} \\ -\sqrt{p} & \sqrt{1-p} \end{pmatrix} \begin{pmatrix} \tilde{Z}_1 \\ Z_2 \end{pmatrix}. \quad (3)$$

The amplitudes,  $Z_i, \tilde{Z}_i$ , are defined in Fig. 2; all  $Z_i, \tilde{Z}_i$  have random phases.

(ii) The orbital action, i.e., magnetic-field-induced curving of trajectories, takes place in the junctions between the point contacts, see Fig. 2. To simplify the action of the junction, we assume that an electron incident, say, from the left, after several bounces [16, 17, 18, 19] off the walls exits either “up” or “down”, i.e., both forward and backward scattering channels are suppressed. This assumption allows us to quantify the bending strength of the junction by a single parameter,  $q$ , which we choose in such a way that  $q = 0$  corresponds to deflection exclusively to the left; for  $q = \frac{1}{2}$  deflections to the left and to the right are equally probable [20]. The relation of  $q$  to the scattering matrix of the junction is the following

$$\begin{pmatrix} Z_2 \\ Z_4 \\ Z_6 \\ Z_8 \end{pmatrix} = \begin{pmatrix} 0 & \sqrt{1-q} & 0 & \sqrt{q} \\ \sqrt{q} & 0 & \sqrt{1-q} & 0 \\ 0 & -\sqrt{q} & 0 & \sqrt{1-q} \\ \sqrt{1-q} & 0 & -\sqrt{q} & 0 \end{pmatrix} \begin{pmatrix} Z_1 \\ Z_3 \\ Z_5 \\ Z_7 \end{pmatrix}. \quad (4)$$

With scattering matrices Eqs. (3), (4) defined, the problem of electron localization by disorder in a magnetic field reduces to the effective network model, which can be studied by transfer-matrix method, similar to directed Chalker-Coddington (CC) model [21], which describes delocalization transition at the point  $H$  in Fig. 1. As in Ref. 21, “unitary” disorder is incorporated via random phases of the link amplitudes,  $Z_i$ . Delocalization transitions in the network define a line on the  $(p, q)$  plane. Important is that this line can be converted into the

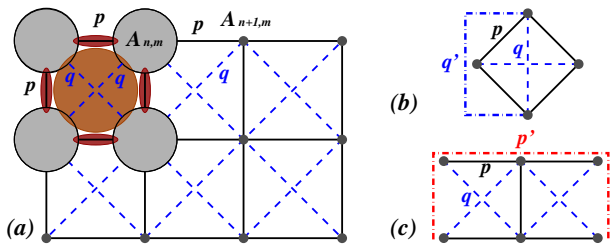


FIG. 5: (Color online) (a) In the classical limit, electron motion reduces to the bond percolation on the lattice consisting of  $p$  and  $q$  -bonds; (b) and (c) are graphic representation of Eqs. (5) and (7), respectively.

dependence  $E_0(\omega_c)$ . Indeed, parameter  $q$  reflects the strength of magnetic field, so that  $(\frac{1}{2} - q) \propto \omega_c$ , while the backscattering probability,  $p$ , decreases monotonously with increasing energy. Thus, the floating scenario is equivalent to the statement that  $p(q)$ -line approaches  $p = 0$  as  $q$  approaches  $\frac{1}{2}$ . Below we argue that the form of  $p(q)$ -line of delocalization transitions is the one shown in Fig. 3(a) (region  $q < \frac{1}{2}$ ), so that it indeed yields the dependence,  $p(q)$ , corresponding to the floating of  $E_0(\omega_c)$ .

In the CC model the transmission of the nodes with “height”,  $E_i$ , and “width”,  $\Gamma$ , is given by the Fermi function [22] by  $T(E, E_i) = \{1 + \exp[(E_i - E)/\Gamma]\}^{-1}$ . Qualitative strong-field picture of the transition [2] emerges when the spread,  $W$ , of heights,  $E_i$ , is much bigger than  $\Gamma$ . Then the quantum interference can be neglected up to large distances,  $\mathcal{R}_{cl} = (W/\Gamma)^{4/3} \gg 1$ , determined by the classical percolation. For smaller distances, one can replace  $T(E, E_i)$  by a step-function,  $\Theta(E_i - E)$ . Adopting the same approach, we assume that in Fig. 2 full transmission takes place in  $p$  percent of point contacts, and full reflection in the rest  $(1 - p)$  percent. Similarly, we assume that a given junction deflects only to the left in  $q^2$  percent of cases, deflects only to the right in  $(1 - q)^2$  percent of cases; in the remaining  $2q(1 - q)$  percent of cases the deflection takes both to the left and to the right depending on incoming channel.

*Phase diagram.* The key observation that allows to establish the phase diagram Fig. 3 is that the classical electron motion over the lattice of point contacts and junctions can be reduced to a single problem of *joint* bond percolation over “ $p$ ” and “ $q$ ” -bonds. To substantiate this statement, we focus on the grey squares in Fig. 2, which are “forbidden” regions for electrons, and notice that electron scattering processes *both* in point contacts and junctions effectively establish bonds between these regions. More specifically, if electron is backscattered in a point contact, we consider that the *centers*  $A_{n,m}$  and  $A_{n,m-1}$  of the squares, adjacent to this contact, are connected by a bond, see Fig. 5. Further, if electron is bent-scattered by a junction, say, in the direction left  $\rightarrow$  down, we identify this process with establishing a bond between the centers of the squares  $A_{n,m}$  and  $A_{n-1,m-1}$ . The above identifi-

cation reduces the classical motion through the network with sites in the centers of squares, see Fig. 5.

*Structure of phases.* We start from the region of strong reflection,  $p > \frac{1}{2}$ . Then the counterpropagating channels in point contacts, Fig. 2, are essentially “short-circuited”. Hence, no delocalization occurs upon increasing magnetic field,  $(\frac{1}{2} - q)$ . Localized states are illustrated schematically in Fig. 4 in the limit  $(1 - p) \ll 1$ . It is apparent that crossover from clockwise rotation (b) to counterclockwise rotation (d) upon passing the zero-field line  $q = \frac{1}{2}$  takes place without delocalization. This absence of delocalization is consistent with low-energy part of Fig. 1, because  $p > \frac{1}{2}$  corresponds to small  $\sigma_0$ . Along the line  $p = \frac{1}{2}$  the  $p$  -bonds alone constitute a critical network. It is seen from Fig. 4 that, as  $p$  is reduced below  $\frac{1}{2}$ ,  $q$  -bonds sustain percolation, manifesting that metallic behavior for  $\sigma_0 > 1$  persists up to strong magnetic fields,  $\omega_c \tau \sim 1$ .

We now turn to the most interesting region of small  $p$  (high energies in Fig. 1). In this domain the overall connectivity of the network is dominated by the  $q$  -bonds. Moreover, at  $p = 0$  the light-blue and dark-blue subnetworks are *completely decoupled*. Small finite  $p$  becomes essential in the vicinity of  $q = \frac{1}{2}$ , when both subnetworks of  $q$  -bonds are critical. Now even weak non-zero  $p$ , by coupling the subnetworks, results in opening of a *metallic* region (e) in the phase diagram. This disorder-induced coupling of critical subnetworks is the fundamental underlying mechanism for the restructuring of states near the point  $L$  in Fig. 1. Since the values  $q > \frac{1}{2}$  are unphysical, the transformation (e)  $\rightarrow$  (a) with increasing magnetic field,  $(\frac{1}{2} - q)$ , is the counterpart of transformation in quantizing magnetic field, which takes place near the point  $H$  in Fig. 1.

Fig. 4 (a) also illustrates that at small  $p$  both subnetworks are chiral. Transformation into the phase (e) upon decreasing magnetic field is accompanied by the change of the Hall conductivity from quantized to finite value smaller than 1. Full suppression of the Hall conductivity in the region (e) occurs only when interference effects drive this region into the Anderson insulator.

*Calculation of positions of the boundaries on the  $(p, q)$ -plane.* Calculation results are shown in Fig. 3(b) and are presented only for  $q < \frac{1}{2}$  due to  $q \rightarrow (1 - q)$  duality. Note, that the end-points  $(p, q) = (0, \frac{1}{2})$  and  $(p, q) = (\frac{1}{2}, 0)$  are conventional bond percolation thresholds. They correspond to percolation over regions with centers in  $A_{m,n}$  connected by  $q$  -bonds and by  $p$  -bonds, respectively, see Fig. 5. Next, the behavior of the boundary at small  $p \ll 1$  can be found perturbatively. Suppose that  $q$  is slightly smaller than  $\frac{1}{2}$ . Then, instead of missing  $q$  -bond, a *pair of one horizontal and one vertical*  $p$  -bonds can provide the connection, see Fig. 5. Resulting shift of the threshold position is determined by the condition

$$f(p, q) = q' = q + 2(1 - q)p^2(1 + q) = \frac{1}{2}, \quad (5)$$

where  $q'$  is the renormalized probability that  $q$ -bond connects, see Fig. 5. Factor 2 accounts for two possibilities to substitute a  $q$ -bond by two  $p$ -bonds.

When  $q$  is small, the role of  $q$ -bonds is to promote percolation over horizontal and vertical bonds. Unlike the previous case, the shift,  $(\frac{1}{2} - p)$ , of the threshold is *linear* in  $q$ . This is because in certain rare cases *one*  $q$ -bond takes on the role of a missing  $p$ -bond. Assume that a vertical  $p$ -bond is absent while one of the neighboring horizontal  $p$ -bonds is present. Then the connection between the end of the missing bonds can be established in two steps: first via this horizontal  $p$ -bond and then via a  $q$ -bond, Fig. 5. More quantitative information about the boundary  $p(q)$  at small  $q$  can be obtained from the real-space renormalization group procedure for bond percolation on the square lattice [23]. According to this procedure probability that a superbond, illustrated in Fig. 5, connects is given by

$$f_0(p) = p^5 + 5p^4(1-p) + 8p^3(1-p)^2 + 2p^2(1-p)^3, \quad (6)$$

where the last three terms correspond to realizations in which superbond connects with one, two, and three original  $p$ -bonds removed. Exact percolation threshold,  $p = \frac{1}{2}$ , emerges in the procedure Ref. 23 as a solution of the equation  $f_0(p) = \frac{1}{2}$ . Note now, that for realizations with two, three, four, or five  $p$ -bonds removed, for which the superbond does not connect, presence of  $q$ -bonds can restore the connectivity. Selecting suitable realizations out of all  $2^4$  possible states of  $q$ -bonds amounts to the following modification of the probability,  $p'$ , that superbond connects

$$f(p, q) = p' = f_0(p) + 10p^2(1-p)^3[2q - q^2] + p(1-p)^4[4q + 8q^2 - 8q^3 + q^4] + (1-p)^5[2q^2 - q^4]. \quad (7)$$

Upon equating  $f(p, q)$  to  $\frac{1}{2}$ , Eq. (7) yields the boundary of percolation transition at small  $q$ . In fact, as seen from Fig. 3(b), the asymptotic behaviors found from Eqs. (5) and (7) match very closely near  $q = \frac{1}{4}$ .

*Localization length.* We have established the form of the phase diagram within classical consideration based on the assumption that the spread of energies of point contacts is large, so that  $\mathcal{R}_{cl} \gg 1$ . Naturally, at distances smaller than  $\mathcal{R}_{cl}$ , where the classical consideration applies, the critical exponent in the domain Fig. 4a is  $\nu = \frac{4}{3}$ . Most interesting domain of floating corresponds to the vicinity of the point  $p = 0$ ,  $q = \frac{1}{2}$ . We expect that, with quantum interference, the phase diagram Fig. 3 will remain unchanged, while metallic phase in Fig. 4e will turn into the Anderson insulator with “unitary” localization length,  $\ln \xi_u = \pi^2 \sigma_0^2$ , where the Drude conductance is related to the parameter,  $p$ , as  $p = c\sigma_0^{-1}$ , with numerical factor  $c \sim 1$ . It will also modify the behavior of localization length,

$$\xi(p, q) \sim \left| f(p, q) - \frac{1}{2} \right|^{-\nu} = \left| \frac{3}{2}p^2 - \left( \frac{1}{2} - q \right) \right|^{-\nu}, \quad (8)$$

in the neighboring insulating region, Fig. 4a, by changing the exponent from classical,  $\nu = \frac{4}{3}$ , to quantum  $\nu = \frac{7}{3}$ . Starting from small field,  $(\frac{1}{2} - q) \ll p^2$ , localization length retains its value  $\xi_u \propto \exp(\pi^2 c^2 / p^2)$  up to the narrow vicinity of the boundary,  $(\frac{1}{2} - q) = \frac{3}{2}p^2$ , when it crosses over to diverging Eq. (8). Relative width of the “quantum” region can be estimated as

$$\frac{\delta \omega_c}{\omega_c} = \frac{\delta \left( \frac{1}{2} - q \right)}{\left( \frac{1}{2} - q \right)} = \frac{1}{p^2} e^{-\frac{3c\pi^2}{7p^2}} = \frac{\sigma_0^2}{c^2} e^{-\frac{3}{7}\pi^2 \sigma_0^2}. \quad (9)$$

Important is that this region progressively narrows as delocalized state floats up. As a final remark, if we assume that  $(\frac{1}{2} - q) \propto \omega_c$  is energy independent, the boundary position  $p = [(1 - 2q)/3]^{1/2}$  translates into  $E_0(\omega_c) \propto \omega_c^{-1/2}$ , while the original prediction [4] is  $E_0(\omega_c) \propto \omega_c^{-1}$ . Note, however, that the prediction [4] is specific for a white-noise disorder.

*Quantum treatment of the network.* Numerical simulations, employing matrices Eqs. (3), (4) for nodes and incorporating random phases into the link amplitudes, are required to verify the above predictions based on the classical picture. These simulations are also supposed to verify the fact that domain  $e$  in Fig. 3 is, quantum-mechanically, insulating. The results of transfer-matrix analysis [24] of the two-channel [25] network Fig. 2 are shown in Fig. 3b for three values of “energy”,  $p$ . As usually, the simulations were performed for a system of width,  $M$ , by imposing periodic boundary conditions in the transverse direction. Upon defining a transfer matrix for a column of  $M$  nodes (a slice), the net transfer matrix of a system of length,  $N$  (typical  $N = 240000$ ), was obtained by multiplying the transfer matrices of  $N$  subsequent slices. Diagonalization of the net transfer matrix yielded the Lyapunov exponents,  $\lambda_i(p, q)$ , related to the eigenvalues as  $\exp(\lambda_i N)$ . Then, localization length,  $\xi_M(p, q)$ , was inferred from the smallest positive exponent:  $\xi_M(p, q) = \lambda_{M/2}^{-1}$ . Each point on the  $(p, q)$ -plane, corresponding to the critical extended state, was identified with  $(p, q)$ -values for which  $\xi_M/M$  becomes  $M$ -independent upon increasing  $M$ . Simulation confidently confirm that for finite “energies”,  $p > 0$ , quantum system is insulating at  $q = 0.5$ , while the state, corresponding to  $p = 0$ ,  $q = 0.5$ , is extended. Despite a good overall agreement, simulation results in Fig. 3b reveal a small but systematic discrepancy between classical and quantum treatments.

*Concluding remarks.* (i) Out of a set,  $E_n(\omega_c)$ , of floating delocalized states [4] we were able to derive only the one with  $n = 0$ . This is because consideration was restricted to two counterpropagating channels in each link. (ii) Among various network models studied [26], the closest to ours is the model [27] describing delocalization in the chiral symmetry class A III. The difference lies in the structure of the node matrices. In particular, classical limit of Ref. 27 corresponds to the asymmetry factor,

$q$ , in left and right incident channels and  $(1 - q)$  for up and down incident channels, Fig. 2. This is how the net chiral symmetry at the nodes is insured in Ref. 27. (iii) Tractable picture of floating scenario was achieved in this paper by neglecting *direct* forward scattering in the junctions. This process is, however, incorporated indirectly, via virtual three-step transition, Fig. 2; its probability is  $\propto p(1 - p)q^2$ .

*Acknowledgments.* This work was supported by the BSF grant No. 2006201.

- 
- [1] B. I. Halperin, Phys. Rev. B **25**, 2185 (1982).  
 [2] R. F. Kazarinov and S. Luryi, Phys. Rev. B **43**, 7626 (1982); S. V. Iordansky, Solid State Commun. **43**, 1 (1982); S. A. Trugman, Phys. Rev. B **27**, 7539 (1983).  
 [3] H. Levine, S. B. Libby, and A. M. M. Pruisken, Phys. Rev. Lett. **51**, 1915 (1983).  
 [4] D. E. Khmel'nitskii, Phys. Lett. **106A**, 182 (1984).  
 [5] H. W. Jiang, C. E. Johnson, K. L. Wang, and S. T. Hannahs, Phys. Rev. Lett. **71**, 1439 (1993).  
 [6] C. E. Johnson and H. W. Jiang, Phys. Rev. B **48**, 2823 (1993).  
 [7] T. Wang, K. P. Clark, G. F. Spencer, A. M. Mack, and W. P. Kirk, Phys. Rev. Lett. **72**, 709 (1994).  
 [8] R. J. F. Hughes, J. T. Nicholls, J. E. F. Frost, E. H. Linfield, M. Pepper, C. J. B. Ford, D. A. Ritchie, G. A. C. Jones, E. Kogan, and M. Kaveh, J. Phys.: Condens. Matter **6**, 4763 (1994).  
 [9] I. Glozman, C. E. Johnson, and H. W. Jiang, Phys. Rev. Lett. **74**, 594 (1995).  
 [10] A. A. Shashkin, G. V. Kravchenko, and V. T. Dolgoplov, JETP Lett. **58**, 220 (1993).  
 [11] M. Hilke, D. Shahar, S. H. Song, D. C. Tsui, Y. H. Xie, and D. Monroe, Phys. Rev. B **56**, R15545 (1997).  
 [12] K. Yang and R. N. Bhatt, Phys. Rev. Lett. **76**, 1316 (1996).  
 [13] see D. N. Sheng, Z. Y. Weng, and X. G. Wen, Phys. Rev. B **64**, 165317 (2001), and references therein.  
 [14] Th. Koschny and L. Schweitzer, Phys. Rev. B **70**, 165301 (2004), and references therein.  
 [15] B. Huckestein, Phys. Rev. Lett. **84**, 3141 (2000).  
 [16] D. G. Ravenhall, H. W. Wyld, and R. L. Schult, Phys. Rev. Lett. **62**, 1780 (1989), R. L. Schult, H. W. Wyld, and D. G. Ravenhall, Phys. Rev. B **41**, 12760 (1990).  
 [17] G. Kirczenow, Phys. Rev. Lett. **62**, 2993 (1989).  
 [18] H. U. Baranger and A. D. Stone, Phys. Rev. Lett. **63**, 414 (1989); H. U. Baranger, D. P. DiVincenzo, R. A. Jalabert, and A. D. Stone, Phys. Rev. B **44**, 10637 (1991).  
 [19] B. Beenakker and H. van Houten, Phys. Rev. Lett. **63**, 1857 (1989).  
 [20] note that similar structure of the node of the network was adopted in Ref. 27 to study delocalization properties in chiral-symmetric class AIII.  
 [21] J. T. Chalker and P. D. Coddington, J. Phys. C **21**, 2665 (1988).  
 [22] H. A. Fertig and B. I. Halperin, Phys. Rev. B **36**, 7969 (1987).  
 [23] P. J. Reynolds, W. Klein, and H. E. Stanley, J. Phys. C **10**, L167 (1977).  
 [24] A. MacKinnon and B. Kramer, Phys. Rev. Lett. **47**, 1546 (1981).  
 [25] V. Kagalovsky, B. Horovitz, and Y. Avishai, Phys. Rev. B **52**, R17044 (1995).  
 [26] B. Kramer, T. Ohtsuki, and S. Kettemann, Phys. Rep. **417**, 211 (2005).  
 [27] M. Bocquet and J. T. Chalker, Phys. Rev. B **67**, 054204 (2003).